AIAA JOURNAL
Vol. 32, No. 9, September 1994

Direct Calculations of Waves in Fluid Flows Using High-Order Compact Difference Scheme

Sheng-Tao Yu*
Sverdrup Technology, Inc., Brook Park, Ohio 44142
and
Lennart S. Hultgren† and Nan-Suey Liu‡
NASA Lewis Research Center, Cleveland, Ohio 44135

The solution of the unsteady Euler equations by a sixth-order compact difference scheme combined with a fourth-order Runge-Kutta method is investigated. Closed-form expressions for the amplification factors and their corresponding dispersion correlations are obtained by Fourier analysis of the fully discretized, two-dimensional Euler equations. The numerical dissipation, dispersion, and anisotropic effects are assessed. It is found that the CFL limit for stable calculations is about 0.8. For a CFL number equal to 0.6, the smallest wavelength which is resolved without numerical damping is about six-eight grid nodes. For phase speeds corresponding to acoustic waves, the corresponding time period is resolved by about 200–300 time steps. Three numerical examples of waves in compressible flow are included: 1) sound propagation in a duct with linear shear, 2) linear wave growth in a compressible free shear layer, and 3) vortex pairing in a compressible free shear layer perturbed at two frequencies.

Introduction

CALCULATION of unsteady flows is of interest because of the applications such as aeroacoustics, flow instability, and direct simulation of turbulent flows. The present paper addresses the numerical issues of simulation of unsteady flows using standard high-order schemes, namely, compact difference for spatial discretization and Runge-Kutta method for time marching.

In Ref. 1, Lele presented various forms of compact difference schemes for applications such as interpolation, filtering, and evaluating high-order derivatives. In previous work,[2] Yu, Tsai, and Hsieh concentrated on the solution of the Euler equations using various combinations of the compact difference (CD) schemes and the Runge-Kutta (RK) methods, and the numerical characteristics were assessed by Fourier analysis of a fully discretized, one-dimensional wave equation. The researchers found significant improvement of the numerical accuracy by using the fourth- or sixth-order compact difference schemes compared to the conventional second-order central difference scheme. In addition, an increase of the order of the RK time marching enlarges the Courant-Friedrichs-Lewy (CFL) limit for stable calculations.

In this paper, we report a further study of the numerical characteristics when using the sixth-order compact difference (CD6) scheme combined with a fourth-order Runge-Kutta method (RK4) to solve the two-dimensional Euler equations. For multidimensional simulations, anisotropic effects, in addition to the dissipation and dispersion errors, must be assessed to estimate the accuracy of the numerical scheme. In contrast to the one-dimensional case, however, no similarity transformation is available to decouple the two-dimensional Euler equations. Consequently, we here apply Fourier analysis directly to the fully discretized, two-dimensional Euler equations. As a result, closed-form expressions for the amplification factors are derived and used to assess the numerical accuracy in terms of dissipation, dispersion, and anisotropic errors.

In the following sections, we first discuss the employed numerical methods. The flow equations discretized by the numerical method are then assessed by the Fourier analysis, in which a closed form of the amplification factor is derived and the dissipation, dispersion, and anisotropy effects are estimated. Finally, to demonstrate the performance of the numerical method, three numerical examples are included in the present paper: sound waves in a duct with linear shear, linear spatial wave growth in a compressible free shear layer, and nonlinear roll up of a compressible free shear layer. In all cases, the numerical simulations show favorable comparison in the linear regime to the corresponding solution of the compressible Rayleigh stability equation. For the nonlinear wave motions, the numerical solutions show crisp resolution of the vortex roll up and pairing.

Numerical Method

The two-dimensional Euler equations in Cartesian coordinates can be cast into a vector form:

$$\frac{\partial Q}{\partial t}+\frac{\partial E}{\partial x}+\frac{\partial F}{\partial y}=0 \tag{1}$$

where Q is the unknown vector and E and F are inviscid fluxes in the x and y directions, respectively. A RK4 method is applied as the temporal discretization and a CD6 scheme is applied to the spatial discretization.

The adopted RK4 method has been used by Jameson et al.[3] to solve the flow equations. The algorithm is given by

$$\begin{aligned} Q^1 &= Q^n+\frac{\Delta t}{2}R^n \\ Q^2 &= Q^n+\frac{\Delta t}{2}R^1 \\ Q^3 &= Q^n+\Delta t R^2 \\ Q^{n+1} &= Q^n+\frac{\Delta t}{6}(R^n+2R^1+2R^2+R^3) \end{aligned} \tag{2}$$

Presented as Paper 93-0148 at the AIAA 31st Aerospace Sciences Meeting, Reno, NV, Jan. 11–14, 1993; received Jan. 30, 1993; revision received Feb. 3, 1994; accepted for publication Feb. 16, 1994. Copyright © 1994 by the American Institute of Aeronautics and Astronautics, Inc. No copyright is asserted in the United States under Title 17, U.S. Code. The U.S. Government has a royalty-free license to exercise all rights under the copyright claimed herein for Governmental purposes. All other rights are reserved by the copyright owner.

*Senior Research Engineer; currently Senior Research Engineer, NYMA Technology, Inc., 2001 Aerospace Parkway, Brook Park, OH 44142.

†Senior Scientist, Lewis Research Academy. Associate Fellow AIAA.

‡Aerospace Engineer, Internal Fluid Mechanics Division. Member AIAA.

The superscripts 1, 2, and 3 denote intermediate steps of the RK method. R^i is the numerical value of $\partial E/\partial x + \partial F/\partial y$ calculated from the flow properties at step i. The algorithm is fourth-order accurate for nonlinear equations and is suitable for the calculations of unsteady flows.

A CD6 scheme is used to spatially discretize the inviscid fluxes. According to Hermite's generalization of the Taylor's series,[4] one can write

$$u'_{i-1} + 3u'_i + u'_{i+1} = \frac{1}{12h}(u_{i+2} + 28u_{i+1} - 28u_{i-1} - u_{i-2}) + \mathcal{O}(h^6) \tag{3}$$

where u is any flow property, the prime represents a spatial derivative, and h is the step size. The present treatment of the transverse and downstream boundary conditions is similar to that in Ref. 2, namely, the fourth-order compact scheme is used at locations one grid node away from the boundary, and a third-order one-sided biased difference scheme is used at the boundary. The one-sided difference scheme incorporates the method of characteristic (MOC) type nonreflecting boundary condition.[2,5] In addition, the numerical grids are stretched near the boundaries to enlarge the computational domain and, as a consequence, the nonreflection effect is enhanced. The application of the CD6 scheme with the aforementioned boundary conditions involves the inversion of a scalar tridiagonal matrix. The inversion of the matrix incurs little penalty in terms of CPU time.

Fourier Analysis

Fourier analysis of a two-dimensional, finite difference scheme assumes that the solution is periodic over an infinite domain with the spatial period equal to the computational domain (L_x and L_y) in the x and y directions, respectively. The computational domain is decomposed into K_x and K_y grid nodes in the x and y directions, respectively. The harmonic content of the discretized equation is limited to the number of grid nodes used in the computational domain. A discrete solution $\boldsymbol{Q}^n_{i,j}$ at a location (i, j) and time (n) is a linear combination of K_x times K_y wave modes. Fourier analysis is performed by substituting each wave mode of the discrete Fourier expansion into the discretized Euler equations to calculate the amplification matrix $\boldsymbol{G}(p,q)$, which is defined as

$$\hat{\boldsymbol{Q}}^{n+1}(p,q) = \boldsymbol{G}(p,q)\hat{\boldsymbol{Q}}^n(p,q) \tag{4}$$

where $\hat{\boldsymbol{Q}}$ denotes the Fourier component of the object function $\boldsymbol{Q}$ and p and q are the wave numbers in the x and y directions, respectively. The amplification factors of the numerical scheme are given by the eigenvalues of $\boldsymbol{G}$, which can simply be obtained by diagonalization of $\boldsymbol{G}$. The procedure is repeated for all wave modes, and the amplification factors over the full spectrum of the wave numbers are obtained. In this process, we map the function $\boldsymbol{Q}$ defined by the spatial coordinates x and y on the domain of $[-L_x/2, L_x/2]$ and $[-L_y/2, L_y/2]$ to the wave number range on $[-\pi, \pi]$ for both p and q. Because of symmetry properties, the results of the Fourier analysis need only be presented in the first quadrant of the (p,q) plane.

To proceed, the generalized form of the amplification matrix $\boldsymbol{G}$ for the RK4 method can be expressed as

$$\boldsymbol{G} = \boldsymbol{I} + \boldsymbol{Z} + \frac{1}{2}\boldsymbol{Z}^2 + \frac{1}{6}\boldsymbol{Z}^3 + \frac{1}{24}\boldsymbol{Z}^4 \tag{5}$$

where $\boldsymbol{I}$ is the identity matrix. $\boldsymbol{Z}$ is the Fourier component of the spatial discretization applied to the convective terms $(-\partial E/\partial x - \partial F/\partial y)$ in the wave number space. To evaluate $\boldsymbol{Z}$, we expand the inviscid fluxes $\boldsymbol{E}$ and $\boldsymbol{F}$ by the chain rule, such as

$$\frac{\partial \boldsymbol{E}}{\partial x} = \frac{\partial \boldsymbol{E}}{\partial \boldsymbol{Q}}\frac{\partial \boldsymbol{Q}}{\partial x} = \boldsymbol{A}\frac{\partial \boldsymbol{Q}}{\partial x}$$
$$\frac{\partial \boldsymbol{F}}{\partial y} = \frac{\partial \boldsymbol{F}}{\partial \boldsymbol{Q}}\frac{\partial \boldsymbol{Q}}{\partial y} = \boldsymbol{B}\frac{\partial \boldsymbol{Q}}{\partial y} \tag{6}$$

where $\boldsymbol{A}$ and $\boldsymbol{B}$ are the Jacobian matrices of the inviscid fluxes. Because the analysis is linear, we linearize Eq. (6) by assuming that $\boldsymbol{A}$ and $\boldsymbol{B}$ are constant. In Ref. 2, the discrete Fourier transformation of $\partial \boldsymbol{Q}/\partial x$ and $\partial \boldsymbol{Q}/\partial y$ are given by

$$F\left(\frac{\partial \boldsymbol{Q}}{\partial x}\right) = -Z_x = -\frac{[4\sin(p)\cos(p) + 56\sin(p)]\Delta t i}{12[2\cos(p) + 3]\Delta x}$$
$$F\left(\frac{\partial \boldsymbol{Q}}{\partial y}\right) = -Z_y = -\frac{[4\sin(q)\cos(q) + 56\sin(q)]\Delta t i}{12[2\cos(q) + 3]\Delta y} \tag{7}$$

where $i = \sqrt{-1}$ and $F(\partial \boldsymbol{Q}/\partial x)$ is the Fourier transformation of the spatially discretized $\partial \boldsymbol{Q}/\partial x$ and is defined as $-Z_x$. As a result, $\boldsymbol{Z}$ can be represented as

$$\boldsymbol{Z} = \boldsymbol{A}Z_x + \boldsymbol{B}Z_y \tag{8}$$

Combination of Eqs. (5), (7), and (8) then gives an expression for the amplification matrix in terms of p and q.

To diagonalize $\boldsymbol{G}$, and thus to obtain its eigenvalues, i.e., the numerical amplification factors of the adopted numerical scheme, we perform a similarity transformation of $\boldsymbol{G}$, namely

$$\boldsymbol{T}^{-1}\boldsymbol{G}\boldsymbol{T} = \boldsymbol{I} + \boldsymbol{T}^{-1}\boldsymbol{Z}\boldsymbol{T} + \frac{1}{2}(\boldsymbol{T}^{-1}\boldsymbol{Z}\boldsymbol{T})^2 + \frac{1}{6}(\boldsymbol{T}^{-1}\boldsymbol{Z}\boldsymbol{T})^3 + \frac{1}{24}(\boldsymbol{T}^{-1}\boldsymbol{Z}\boldsymbol{T})^4 \tag{9}$$

The matrices $\boldsymbol{T}^{-1}$ and $\boldsymbol{T}$ which diagonalize $\boldsymbol{G}$ are given by

$$\boldsymbol{T}^{-1} = \begin{bmatrix} 1 & 0 & 0 & -1/c^2 \\ 0 & \beta & -\alpha & 0 \\ 0 & \alpha/\sqrt{2} & \beta/\sqrt{2} & 1/(\sqrt{2}\rho c) \\ 0 & -\alpha/\sqrt{2} & -\beta/\sqrt{2} & 1/(\sqrt{2}\rho c) \end{bmatrix} \tag{10}$$

$$\boldsymbol{T} = \begin{bmatrix} 1 & 0 & \rho/(\sqrt{2}c) & \rho/(\sqrt{2}c) \\ 0 & \beta & \alpha/\sqrt{2} & -\alpha/\sqrt{2} \\ 0 & -\alpha & \beta/\sqrt{2} & -\beta/\sqrt{2} \\ 0 & 0 & \rho c/\sqrt{2} & \rho c/\sqrt{2} \end{bmatrix} \tag{11}$$

where ρ is density, c is the speed of sound, $\alpha = Z_x/(Z_x^2 + Z_y^2)^{1/2}$, and $\beta = Z_y/(Z_x^2 + Z_y^2)^{1/2}$. The ℓth row of $\boldsymbol{T}^{-1}$ is the ℓth left eigenvector of $\boldsymbol{G}$, corresponding to the eigenvalue g_ℓ. Finally, the amplification factor g_ℓ is

$$g_\ell = 1 + \lambda_\ell + \frac{1}{2}\lambda_\ell^2 + \frac{1}{6}\lambda_\ell^3 + \frac{1}{24}\lambda_\ell^4 \tag{12}$$

where $\ell = 1, \ldots, 4$ and λ_ℓ is the ℓth eigenvalue of the matrix $Z_x\boldsymbol{A} + Z_y\boldsymbol{B}$ which is also diagonalized by $\boldsymbol{T}^{-1}$ and $\boldsymbol{T}$, and are given by

$$\lambda_1 = Z_x u + Z_y v$$
$$\lambda_2 = Z_x u + Z_y v$$
$$\lambda_3 = Z_x u + Z_y v + c(Z_x^2 + Z_y^2)^{1/2}$$
$$\lambda_4 = Z_x u + Z_y v - c(Z_x^2 + Z_y^2)^{1/2} \tag{13}$$

Equation (13) shows that there are only three distinct amplification factors representing three kinds of numerical waves propagating in the dispersive numerical medium, namely, $g_{1,2}$, g_3, and g_4 waves. As shown in Eqs. (12) and (13), $g_{1,2}$ represents the numerical waves simulating the flow velocity. Specifically, the velocity vector (u, v) is modulated by a inner product with the vector (Z_x, Z_y) due to the spatial discretization. The numerical wave is further modulated by substituting the inner product into Eq. (12) for the RK4 method to obtain the amplification factors. Similarly, g_3 and g_4 waves are the numerical counterparts of the acoustic waves superimposed on the flow motion. Unlike the flow velocity waves, however, the acoustic waves propagate in all directions from a moving source and the phase speed c is modulated by the factor $(Z_x^2 + Z_y^2)^{1/2}$.

The amplification factors can be written in the form

$$g_\ell(p,q) = |g_\ell(p,q)|e^{i\alpha(p,q)} \tag{14}$$

and we can make the following interpretations:

1) Artificial dissipation: The $|g_\ell(p,q)|$ represents the numerical amplification, i.e., when $|g| \geq 1$, the scheme is unstable. For calculations of unsteady flows, we want $|g|$ to be less than and close to unity to ensure numerical stability with minimum artificial dissipation. We will show $|g(p,q)|$ against p and q to illustrate the artificial dissipation.

2) Artificial dispersion: The $\alpha(p,q)$ represents the artificial dispersion. We will show contours of constant α hereafter to indicate phase velocities which in turn are used to estimate the artificial dispersion.

3) Artificial anisotropy: Certain directions of wave propagation will be favored by the numerical scheme. Changes of the flow direction (u and v) allow us to assess the anisotropy of $q_{1,2}$. For the simulated acoustic ($q_{3,4}$) waves, the flow velocity is turned off when assessing their isotropy.

Figure 1 shows the artificial dissipation of three different numerical waves represented by $|g_{1,2}|$, $|g_3|$, and $|g_4|$. To obtain the numerical values, u, v, and c are specified. Here, u is set to be equal to v and the flow velocity is at 45 deg to the coordinate axes. The magnitude of the flow speed is set to be equal to c, i.e, $M = 1$. As shown in Fig. 1, there is negligible dissipation of $|g_{1,2}|$ and $|g_4|$. On the contrary, $|g_3|$ shows significant dissipation at moderate wave numbers. The minima of $|g_{2,3,4}|$ are 0.98, 0.51, and 0.99, respectively. Therefore, acoustic waves propagating along the same direction as

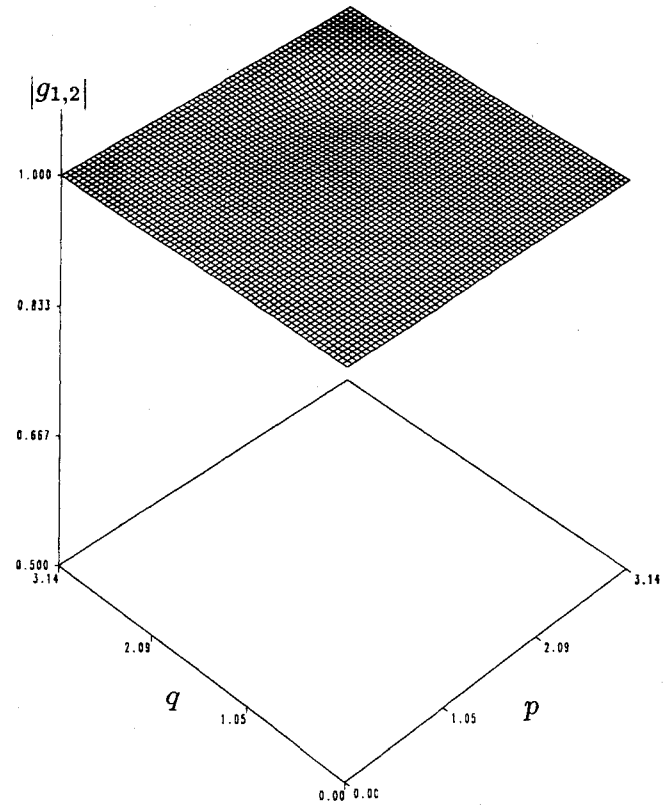

a) $|g_{1,2}(p, q)|$ for $u = v$ and $c = \sqrt{u^2 + v^2}$

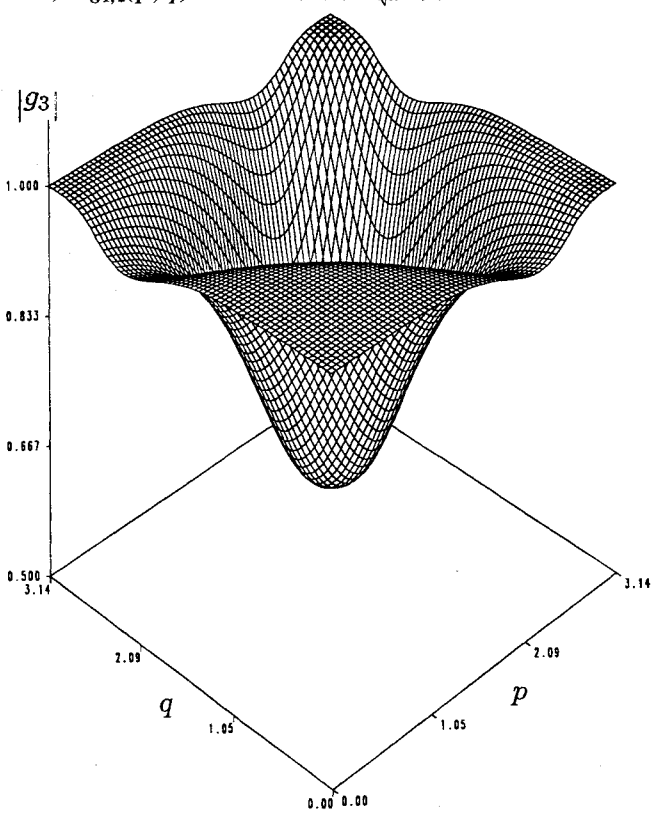

b) $|g_3(p, q)|$ for $u = v$ and $c = \sqrt{u^2 + v^2}$

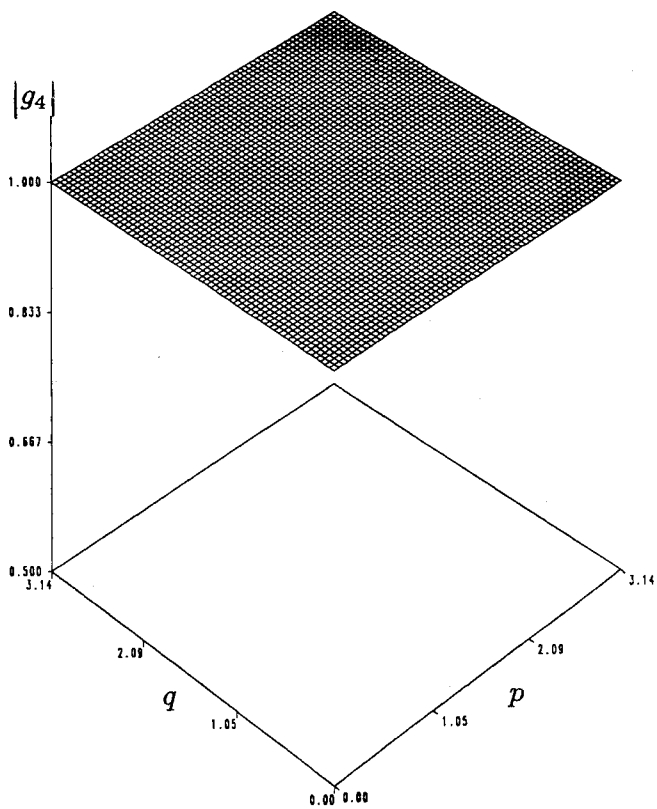

c) $|g_4(p, q)|$ for $u = v$ and $c = \sqrt{u^2 + v^2}$

Fig. 1 Dissipation of the CD6-RK4 scheme for CFL = 0.6.

the flow motion suffer from the worst dissipative error. For lower speed flows ($M \leq 1$), the dissipation effect is less severe and the minimum of $|g_3|$ is larger than 0.51. As a contrast, for supersonic flows, more dissipation in the flow direction is anticipated as compared to that shown in Fig. 1. As a result, we defined the critical CFL number by

$$\mathrm{CFL}_c = \max\{\ |Z_x u + Z_y v + c(Z_x^2 + Z_y^2)^{1/2}|$$

$$|Z_x u + Z_y v - c(Z_x^2 + Z_y^2)^{1/2}|\ \} \times \frac{\Delta t}{\sqrt{\Delta x^2 + \Delta y^2}} \qquad (15)$$

For this case, CFL_c is 0.6. In Fig. 1b (dissipation of g_3), there is negligible dissipation in the low wave number region, i.e., $p,q \leq \pi/3$. This region corresponds to waves with wavelengths greater than six grid nodes. Note that little dissipation is also observed in the other three corners of the same plot. For example, for $p,q = \pi$ which is wave resolved by two grid nodes (or even-odd wave) in both the x and y directions, there is essentially no artificial dissipation. Later on, we shall show that these waves are undesirable due to significant dispersive errors. Although not shown, it is noted that for CFL_c greater than 0.8, $|g_3(p,q)|$ becomes larger than unity at certain p and q and the calculation is numerically unstable. Therefore, the CFL_c limit is 0.8 and a value between 0.5 and 0.7 is recommended for accurate calculations. Although the current calculation assumes that the Mach number is unity, it is noted that the stability criterion remains approximately the same for other flow speeds.

Figure 2 shows constant α contours by which numerical phase velocities can be interpreted. The phase velocity vectors point in the direction normal to the contours. The distance between the consecutive contours is an indication of the magnitude of the phase velocity; an increase of the distance is a decrease of the phase velocity and vice versa. Figure 2a shows the phase velocities of the $g_{1,2}$ waves, i.e., flow velocity waves. In this case, the flow direction is 45 deg. The region in which the phase velocities are correctly simulated by the numerical scheme is circumscribed by a dashed line. Outside this region, the phase velocities are in erroneous directions. Similar to the dissipation error, there is little dispersive error for $p,q \leq \pi/3$. To assess the anisotropic effect, Fig. 2b shows the phase velocities of the $g_{1,2}$ waves at 22.5 deg to the x axis. Inside the dashed line, the waves are well resolved. Again, in the low wave number region ($p,q \leq \pi/3$), there is little dispersive error. Figures 2c and 2d show the phase velocities of the simulated acoustic waves superimposed on the flow stream at 45 deg.

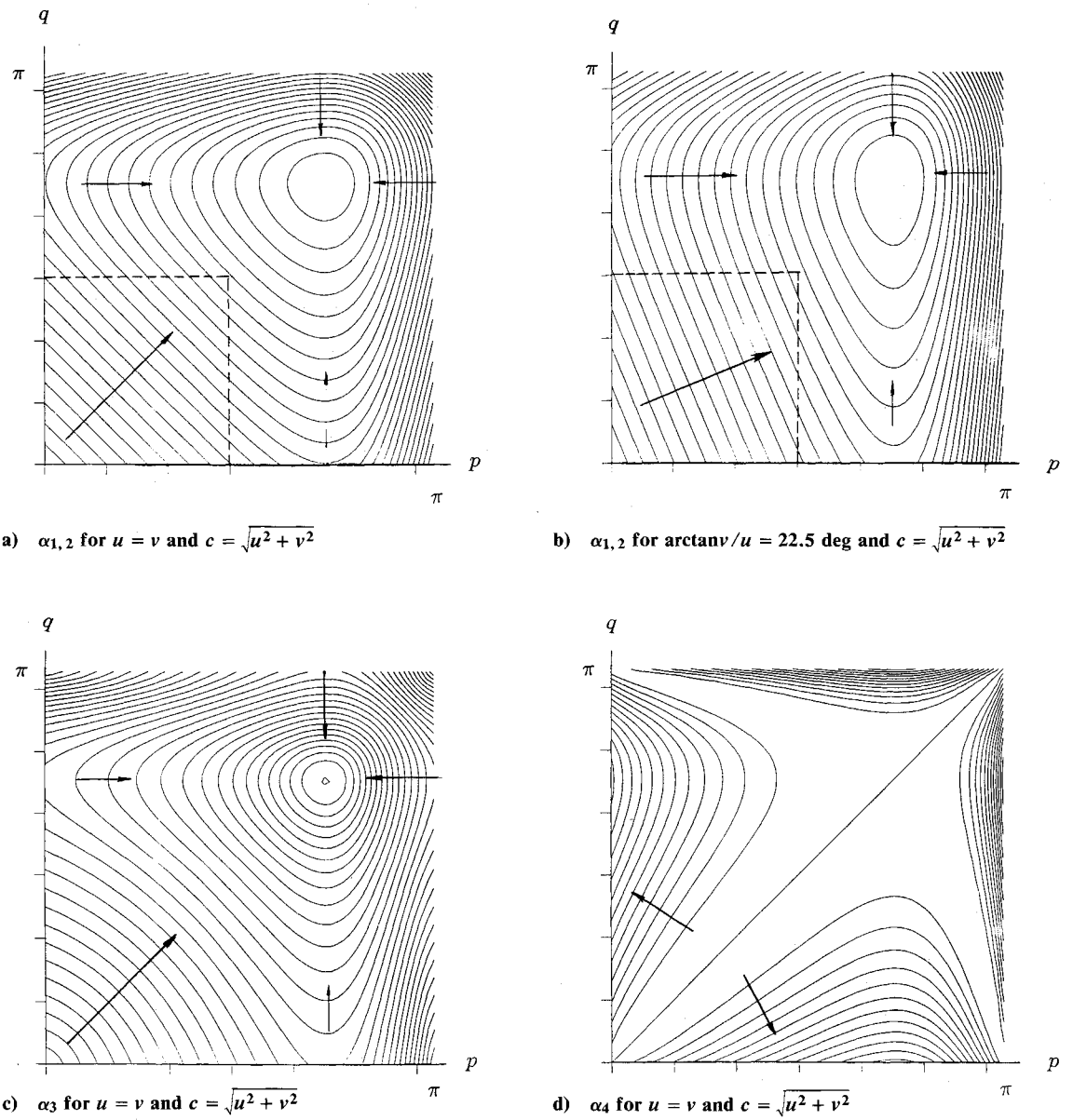

a) $\alpha_{1,2}$ for $u = v$ and $c = \sqrt{u^2 + v^2}$

b) $\alpha_{1,2}$ for $\arctan v/u = 22.5$ deg and $c = \sqrt{u^2 + v^2}$

c) α_3 for $u = v$ and $c = \sqrt{u^2 + v^2}$

d) α_4 for $u = v$ and $c = \sqrt{u^2 + v^2}$

Fig. 2 Dispersion of the CD6-RK4 scheme for CFL = 0.6.

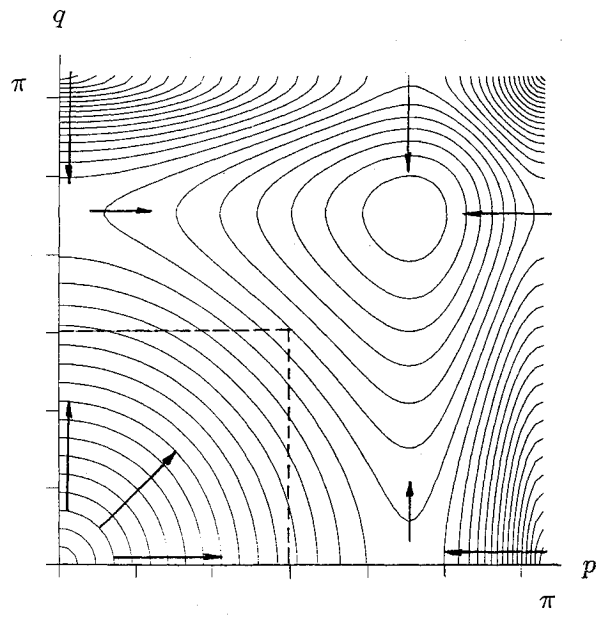

Fig. 3 Dispersion characteristics of the acoustic waves using the CD6-RK4 scheme for CFL = 0.6.

Perhaps it is helpful to temporarily turn off the flow velocity to observe the acoustic velocities alone as shown in Fig. 3. Theoretically, the propagation of the acoustic waves is isotropic and is depicted by circular contours of constant α. Again, the well-resolved region is circumscribed by a dashed line; outside the dashed line, acoustic waves propagate in the wrong directions with erroneous magnitude. For long wavelengths (at least six grid nodes), little preference of the propagation direction of the acoustic wave is observed; there is no evidence of any anisotropic error. Outside the circumscribed region, however, the figure shows an increase of separation between contours along the coordinate axes to a maximum, followed by a decrease. This indicates that the acoustic waves of moderately high wave numbers propagate too slowly along the numerical grid lines. At very high wave numbers, the acoustic waves travel in the opposite direction than they should.

As was discussed earlier, the CD6-RK4 scheme has no dissipative effects at the high wave numbers. However, significant dispersive and anisotropic errors are associated with these wave numbers. Throughout the course of a numerical simulation, these high-wave-number waves propagate with erroneous directions and phase speeds, and will eventually destroy the solution. Therefore, it is appropriate to impose a small amount of high-order artificial damping to filter out these waves, at the same time keeping the resolution at low wave modes intact. The eighth-order artificial damping, defined as

$$\text{A.D.} = \frac{\eta}{8}\left[-u_{i+4} - u_{i-4} + 8(u_{i+3} - u_{i-3}) - 28(u_{i+2} + u_{i-2}) + 56(u_{i+1} + u_{i-1}) - 70u_i\right] \tag{16}$$

is recommended. In the present applications, $\eta = 0.003$ is used.

Numerical Examples

Sound Waves in a Duct with Linear Shear

Our first example is that of a forced sound wave propagating in a two-dimensional duct with linear shear and constant mean temperature. The corresponding linearized problem has been addressed by Pridmore-Brown.[6] Previously, a similar calculation was carried out by Hsieh[7] using another finite difference scheme. For a constant mean temperature, the compressible Rayleigh equation can be expressed as

$$\frac{d^2\hat{p}}{dy^2} + \frac{2\kappa M'}{1 - \kappa M}\frac{d\hat{p}}{dy} + k^2[(1 - \kappa M)^2 - \kappa^2]\,\hat{p} = 0 \tag{17}$$

where $M = M_1 U(y)$, $k = M_1\omega/\sqrt{T_o}$, $\kappa = \sqrt{T_o}/M_1 c$, and T_o is the constant mean-flow temperature. $M(y)$ is the local Mach number of the mean flow; k and $1/\kappa$ are the angular frequency and the phase speed, both made nondimensional using the speed of sound as reference velocity. Equation (17) is to be solved subject to the boundary conditions

$$\frac{d\hat{p}}{dy} = 0 \quad \text{at} \quad y = 0 \quad \text{and} \quad y = 1 \tag{18}$$

For a given angular frequency k, Pridmore-Brown[6] solved the preceding eigenvalue problem using an asymptotic procedure valid for small κ. In this report, we numerically solve the eigenvalue problem by using a finite difference method instead. Briefly, by using second-order central difference approximations for the derivatives in Eq. (17) and second-order forward and backward difference approximations in Eq. (18), the problem is converted into a matrix eigenvalue problem of the form

$$[A]_0 f + \kappa[A]_1 f + \kappa^2[A]_2 f + \kappa^3[A]_3 f = 0 \tag{19}$$

where $[A]_i$ $(i = 0, \ldots, 3)$ are $P \times P$ coefficient matrices and the elements of the column vector f represent the discrete solution at the grid points. Equation (19) is a polynomial type matrix eigenvalue problem. We used the standard QZ algorithm to calculate the eigenvalues κ_i $(i = 1, \ldots, P)$. The numerical convergence was checked by doubling the number of grid nodes.

For the present comparison with the numerical simulation, the Mach number distribution of the mean flow was taken to vary linearly from null to a half across the stream. With $k = 2\pi$, the eigenvalue corresponding to the lowest mode of

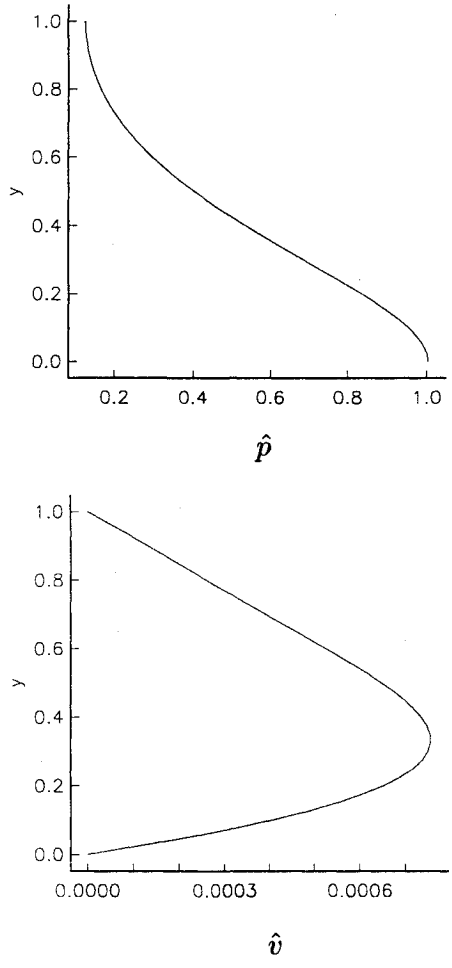

Fig. 4 Theoretical eigenfunction components p' and v' for acoustic waves in a duct with linear shear.

propagation was found to be $\kappa = 0.842758$. The streamwise wavelength of the forced perturbation is then $1/\kappa$ (about 1.19 channel heights). The streamwise length of the computational domain was selected to be five channel heights and the whole domain was subdivided into 200×40 uniformly distributed grid nodes. The maximum magnitude of the perturbation was taken to be one one-hundredth. Figure 4 shows the eigenfunction components corresponding to the pressure and velocity perturbations as functions of y. These eigenfunctions in conjunction with the prescribed frequency k were used as the upstream perturbation for the computational fluid dynamics (CFD) calculation. Figure 5 shows the reconstructed eigenfunctions of p' at two, three, and four wavelengths downstream of the forced perturbation. In the figure, the solid line is the theoretical linear solution. Less than a 5% error is observed at the farthest downstream location. We also observe much larger pressure fluctuations near the lower wall; this can be interpreted as refraction by the mean-flow gradient.

Linear Wave Growth in a Free Shear Layer

A free shear layer is composed of two flow streams in the same direction but with different speeds. Small upstream perturbations are selectively amplified by the free shear layer and grow exponentially in the linear regime. These spatially growing instability waves cause vortex roll up and merging at the further downstream of the flow development.

The flow properties of the fast stream are used here as reference scales and all properties have been nondimensionalized accordingly in the following equations. In addition, the length scale is taken as $\delta/2$ where δ is the vorticity thickness and is defined as

$$\delta = (U_{1*} - U_{2*})/\left(\frac{dU_*}{dy_*}\right)\max \tag{20}$$

where the star denotes the dimensional properties.

For a sufficiently large value of the Reynolds number, the mean-flow pressure can be assumed uniform across the shear layer and the mean-flow velocity in the transverse direction V can, for the purpose of analyzing the unsteady motion, be set to null. A reasonable model for the streamwise mean-flow velocity distribution is provided by

$$U(y) = \frac{1 + R \tanh y}{1 + R} \tag{21}$$

where $R = (U_{1*} - U_{2*})/(U_{1*} + U_{2*})$ is commonly known as the velocity ratio of the shear layer. For simplicity, the Prandtl

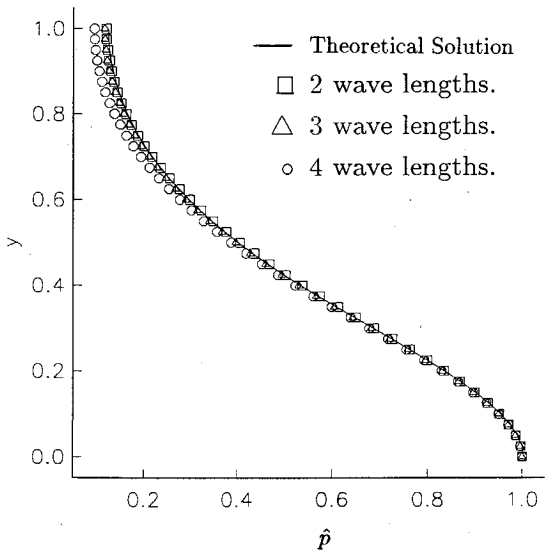

Fig. 5 Reconstructed eigenfunction of p' from the CDF results using the CD6-RK4 method for acoustic waves in a duct with linear shear.

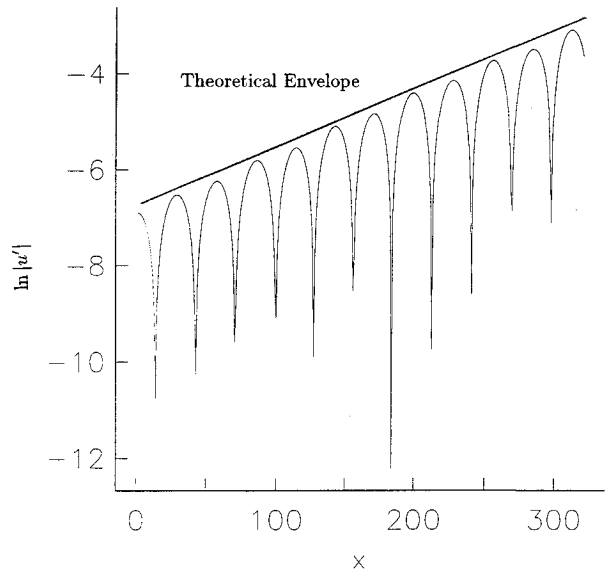

Fig. 6 Instantaneous distribution of $|u'|$ along the center line of the free shear layer.

number is taken to be unity and the mean-flow temperature distribution can then be obtained from the Buseman-Crocco relationship.[8]

In this case, a shooting method was used to obtain the spatial eigenvalues of the Rayleigh stability problem. The mean-flow conditions are $M_1 = 1.5$, $R = 0.15$, and $T_2 = 1.85$, and the boundary condition is that $\hat{p}$ remains bounded as $y \to \pm\infty$. The solution provides a set of viable data of α_i for the corresponding ω.

We choose the case of $\omega = 0.10101$, with the corresponding growth rate of $\alpha_i = -0.012445$, for the CFD calculation. The chosen ω and the corresponding eigenfunction components are used as the imposed harmonic perturbation at the upstream boundary. Note that the eigenfunctions are complex and, therefore, the upstream perturbation is of the form,

$$\phi' = \hat{\phi}_r(y) \cos(\omega t) - \hat{\phi}_i(y) \sin(\omega t) \tag{22}$$

where ϕ' represents u', v', p', or ρ'. Because there are four governing equations, only four boundary conditions need to be prescribed for the numerical simulation. The fluctuations of other flow properties at the upstream boundary, e.g., temperature, are automatically contained in the equation set. The magnitude of the perturbation is set by specifying the transverse maximum rms value of the streamwise velocity perturbation, and this magnitude is taken to be one thousandth.

The computational domain is divided into a 700×70 mesh. The flow domain along the streamwise direction covers about six wavelengths of the imposed perturbation. The numerical grid is clustered in the transverse direction near the center to provide high resolution of the flowfield. Figure 6 shows an instantaneous distribution of $|u'|$ along the center line of the shear layer. The abscissa is the normalized streamwise distance and the ordinate is the normalized $|u'|$ plotted in natural log scale. As shown in the figure, the growth rate of the wave is linear (in the log scale) and the envelope slope is within 3% of the spatial growth rate $(-\alpha_i)$ predicted by the linear stability theory. Because the imposed upstream harmonic perturbation is an eigenfunction of the linear spatial stability problem, the linear exponential growth of the disturbance in the numerical simulation starts from the very beginning of the computational domain; no transitional region is observed in the vicinity of the upstream boundary.

Figure 7 shows the normalized modulus of the reconstructed eigenfunction components u' and p' at various downstream locations compared to the corresponding prescribed quantities. Note that each component has been normalized sepa-

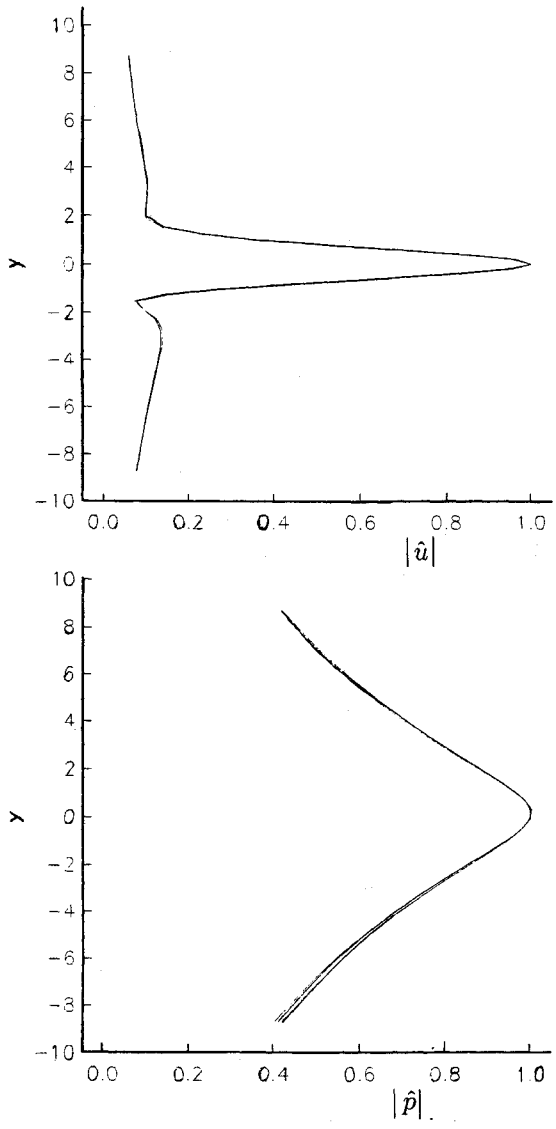

Fig. 7 Reconstructed eigenfunction components u' and p' from the CFD results for the compressible shear layer.

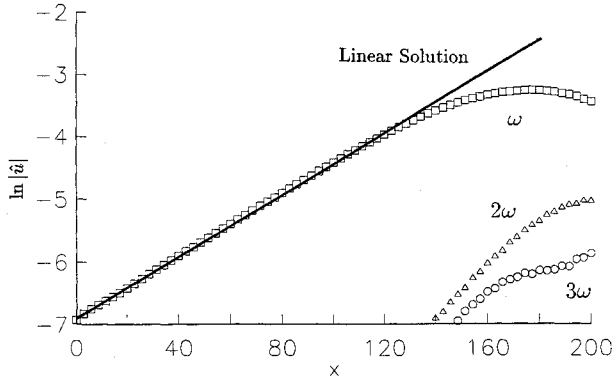

Fig. 8 Fourier coefficients of the unsteady motion in a compressible free shear layer perturbed by the most unstable mode at a magnitude of one thousandth.

rately here by its maximum value. It is obvious that the CD6-RK4 finite difference method faithfully preserves the functional shape of the original perturbation.

Rollup of a Compressible Free Shear Layer

The mean-flow conditions for the present calculation are taken to be the same as in case 2. The angular frequency of the imposed disturbance at the upstream boundary is taken to correspond to the most unstable mode, however. Thus, $\omega = 0.389$ which corresponds to a spatial growth rate $\alpha_i = -0.026067$. First, a magnitude of one one-thousandth is used to verify the linear growth (in the natural log scale) of the instability wave. By doing so, two particular conditions in the unstable angular frequency range, one corresponding to a relatively long wave mode (case 2) with a moderate growth rate and the other to the most unstable mode, are used to demonstrate or assess the accuracy of the finite difference

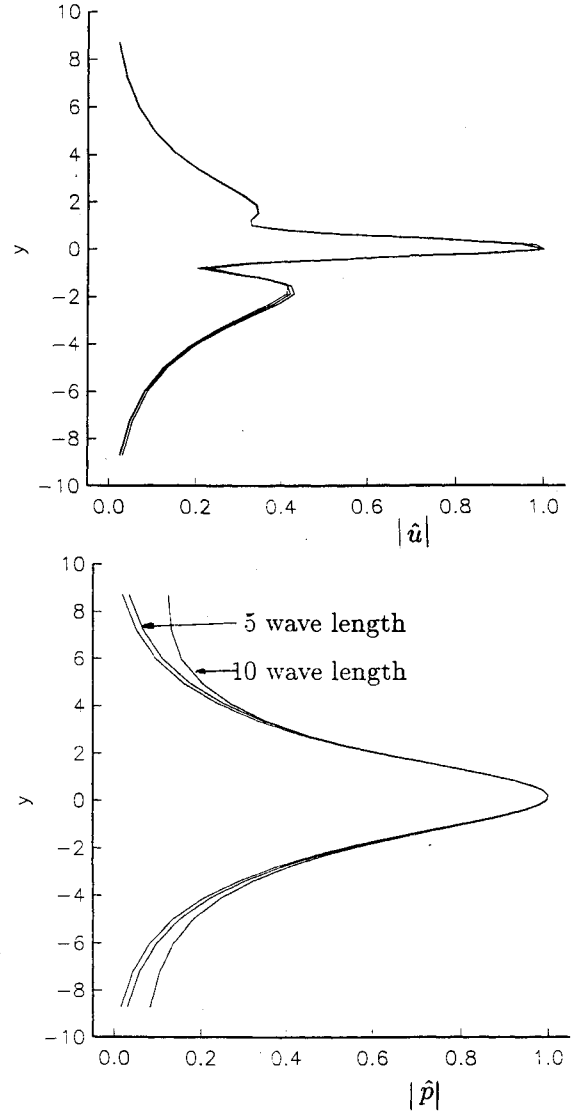

Fig. 9 Reconstructed eigenfunction components u' and p' from the CFD results for the free shear layer perturbed by the most unstable mode.

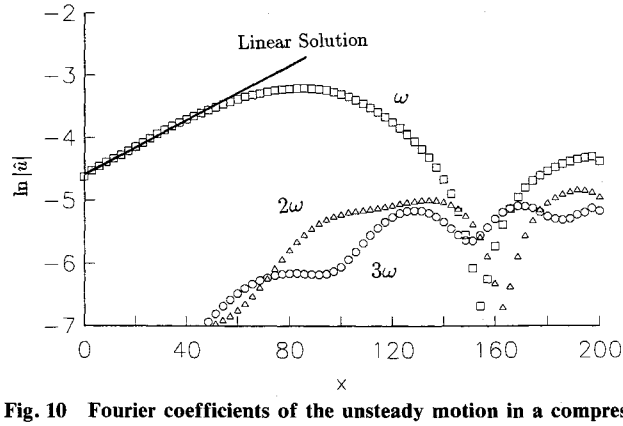

Fig. 10 Fourier coefficients of the unsteady motion in a compressible free shear layer perturbed by the most unstable mode at a magnitude of one hundredth.

Fig. 11 Contours of constant vorticity of the simulated free shear layer perturbed by the most unstable mode at a magnitude of one hundredth.

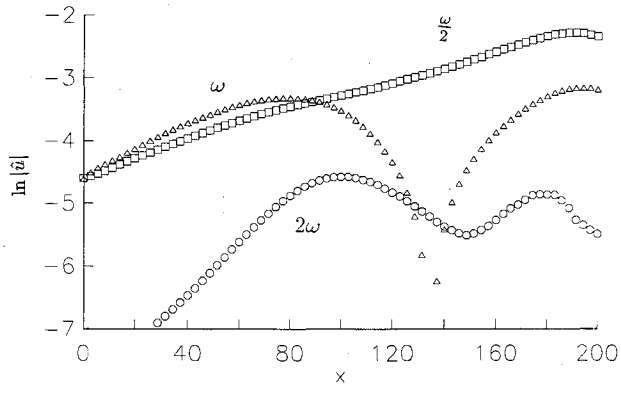

Fig. 12 Fourier coefficients of the unsteady motion in a compressible free shear layer perturbed by the most unstable mode and its subharmonic.

Fig. 13 Contours of constant vorticity of the simulated free shear layer perturbed by the most unstable mode and its subharmonic.

scheme in simulating linear waves. Second, we increase the magnitude of the perturbation to illustrate the vortex rollup. Finally, the subharmonic of the most unstable mode is imposed in addition to the most unstable mode at the upstream boundary. As in the single-frequency case, the transverse structure of the upstream harmonic forcing is given by the corresponding components of both the fundamental and subharmonic linear eigenfunctions to ensure that no undesirable perturbation is introduced into the system.

Figure 8 shows the streamwise variation of the Fourier coefficients of u' along the center line of the free shear layer obtained by a spectral analysis of the numerical simulation. This figure clearly shows the linear growth (in the natural log scale) of the most unstable mode in the initial phase of the flow development. The slope of the curve compares favorably with the theoretical linear growth. At the further downstream nonlinear stage of the flow development, higher harmonics are generated as a prelude to the vortex rollup and, in addition, the growth of the fundamental mode stalls. Figure 9 shows the reconstructed distributions of u' and p' as compared to the corresponding theoretical linear eigenfunctions at downstream stations. For the streamwise location at 10 wavelengths, the flow is weakly nonlinear and the disturbance shows some deviation from the linear-theory prediction.

Figure 10 shows the streamwise variation of the the Fourier coefficients of u' with the larger forcing magnitude of one hundredth. The linear growth of the instability wave is now limited to a region in the vicinity of the upstream boundary. At the further downstream stations, the shear layer has rolled up as can be seen in Fig. 11, where constant-vorticity contours are plotted. The nonlinear redistribution of the unsteady vorticity that occurs during the roll-up process alters the energy transfer from the mean flow to the disturbance and is thus responsible for the saturation of the instability-wave amplitude seen in Fig. 10. In addition, at $x = 160$, all three harmonic modes experience significant reduction. This is an indication of the onset of the strong nonlinear mechanism, in which the background flow used for the eigenvalue problem is severely distorted. Consequently, the flow energy is distributed to other Fourier modes, which are unrelated to the original eigenvalue problem.

Finally, a two-frequency perturbation is imposed at the upstream boundary. The magnitudes of both the fundamental and its subharmonic are set to be one hundredth and the phase difference between the two components were taken to be zero. Figure 12 shows the streamwise variations of the Fourier coefficients of u' corresponding to the fundamental (ω), second harmonic (2ω), and subharmonic ($\omega/2$). The growth rates of both the fundamental and its subharmonic accurately mimic the theoretical results in the initial linear region. Compared to Fig. 10, Fig. 12 shows an earlier appearance of the 2ω harmonic. This is indicative of an earlier rollup in this case. Figure 13 shows the constant-vorticity contours for this case. Due to the presence of the subharmonic, the vortex pairing process has been initiated within the computational domain.

Concluding Remarks

In this paper, the performance of the CD6-RK4 finite difference method in simulating linear and nonlinear wave motions in shear layers has been investigated. The numerical scheme is assessed in terms of the numerical dissipation, dispersion, and anisotropic effects and by numerical examples.

Fourier analysis of the fully discretized, two-dimensional Euler equations led to closed-form expressions for the amplification factors. It is found that there are three groups of numerical waves propagating in the numerically dispersive medium, namely, the flow velocity waves and two acoustic waves superimposed on the flow velocity. Although only the acoustic wave that propagates in the direction of the flow velocity suffers from significant dissipation errors, all three groups of waves suffer from dispersive errors at high wave numbers. For the present scheme, the CFL number limit for stable and accurate calculations is about 0.8. Under the CFL limit, dissipation, dispersive, and anisotropic artifacts are negligible for wave numbers less than $\pi/3$ which corresponds to waves resolved by more than six grid nodes.

Three numerical examples of waves in compressible flows are presented: 1) sound propagation in a duct with linear shear and constant temperature, 2) wave growth in a two-dimensional, compressible free shear layer, and 3) vortex pairing in a compressible free shear layer perturbed by dual frequencies. The results compare favorably to the theoretical solutions for linear wave motions. For nonlinear waves, the CFD results provide crisp resolution of the appearance of higher harmonics, modulation of wave modes, vortex rollup, and vortex pairing.

Acknowledgments

The support of the present research by NASA Lewis Research Center, under Contract NAS 3-25266, monitored by R. M. Stubbs, is greatly appreciated. The first author benefited from discussions with K. C. Hsieh of Sverdrup technology, Inc., NASA Lewis Group, and Z. Yang of the Center for Modeling of Turbulence and Transition of the Ohio Aerospace Institute regarding the first numerical example.

References

[1]Lele, S. K., "Compact Finite Difference Schemes with Spectral-Like Resolution," *Journal of Computational Physics,* Vol. 103, Nov. 1992, pp. 16–42.

[2]Yu, S. T., Tsai, Y.-L. P., and Hsieh, K. C., "Runge-Kutta Methods Combined with Compact Difference Schemes for the Unsteady Euler Equations," AIAA Paper 92-3210, June 1992.

[3]Jameson, A., Schmidt, W., and Turkel, E., "Numerical Solutions of the Euler Equations by Finite Volume Methods Using Runge-Kutta Time-Stepping Schemes," AIAA Paper 81-1259, Jan. 1981.

[4]Colatz, L., *The Numerical Treatment of Differential Equations,* Springer-Verlag, New York, 1966, pp. 538–539.

[5]Giles, M. B., "Nonreflecting Boundary Conditions for Euler Equation Calculations," *AIAA Journal,* Vol. 28, No. 12, 1990, pp. 2050–2059.

[6]Pridmore-Brown, D. C., "Sound Propagation in a Fluid Flowing Through an Attenuating Duct," *Journal of Fluid Mechanics,* Vol. 4, July 1958, pp. 393–406.

[7]Hsieh, K. C., "Assessment of Numerical Techniques for Unsteady Flow Calculations," AIAA Paper 89-1956, June 1989.

[8]Liepmann, H. W., and Roshko, A., *Elements of Gasdynamics,* Wiley, New York, 1957, p. 193.